



JGR Solid Earth

RESEARCH ARTICLE

10.1029/2020JB019421

Key Points:

- Interannual-to-decadal variation of Earth's oblateness J_2 is primarily caused by climatic meridional mass transports.
- We find significant correlation and its frequency dependence of ΔJ_2 with climatic oscillations of AO, AAO and PDO.
- We analyze the decadal 18.61-year tidal ΔJ_2 and report a ~10.5-year ΔJ_2 variability of unidentified origin.

Correspondence to:

B. F. Chao,
bfchao@earth.sinica.edu.tw

Citation:

Chao, B. F., Yu, Y., & Chung, C. H. (2020). Variation of Earth's oblateness J_2 on interannual-to-decadal timescales. *Journal of Geophysical Research: Solid Earth*, 125, e2020JB019421. <https://doi.org/10.1029/2020JB019421>

Received 16 JAN 2020

Accepted 9 MAY 2020

Accepted article online 13 MAY 2020

Variation of Earth's Oblateness J_2 on Interannual-to-Decadal Timescales

B. F. Chao¹ , Y. Yu^{1,2}, and C. H. Chung^{1,3} 

¹Institute of Earth Sciences, Academia Sinica, Taipei, Taiwan, ²Scripps Institution of Oceanography, University of California, San Diego, La Jolla, CA, USA, ³Department of Geosciences, National Taiwan University, Taipei, Taiwan

Abstract The Earth's oblateness varies slightly due to a host of physical processes that involve large-scale meridional N-S mass redistributions in the Earth. We analyze these minute, broadband signals in the observed ΔJ_2 data series for 1976–2019 (43 years). We first remove the near-quadratic variation (due to the glacial isostatic adjustment plus the accelerating land ice melting) and the seasonal terms (due to seasonality of the surface geophysical fluids) by least squares regression. Then we examine via cross-correlation function and cross-coherence spectrum the relationships of the remaining interannual-to-decadal ΔJ_2 with various climate oscillations in terms of their respective indices. We elucidate the contributions of the Antarctic Oscillation and Arctic Oscillation (for timescales shorter than 5 years), Pacific Decadal Oscillation (for timescales longer than 5 years), and the absence thereof in El Niño–Southern Oscillation and Atlantic Multidecadal Oscillation. Removal of their contributions from ΔJ_2 reveals two remaining, nonclimatic long-period signals: An 18.61-year tidal signal calls for an augmentation in the in-phase value and a reduction of the out-of-phase value in the theoretical models per International Earth rotation and Reference systems Service (IERS), while a more detailed quantitative study awaits future, longer data. An additional 10.5-year signal is found to be correlated with the solar cycle, but the origin of this apparent correlation is uncertain presently.

1. Introduction

A long-term axial spin causes the Earth to take a spheroidal shape (Chandrasekhar, 1933). The resultant ellipsoidal flattening of the Earth amounts to about 1 part in 300. This shape is a result of the hydrostatic balance between the dominant gravitational force, that wants to pull the Earth into a minimum-energy configuration of spherical symmetry, against the centrifugal force arising from Earth's rotation, which tends to expel mass away from the rotating axis. The ratio of the (equatorial) centrifugal force to the surface gravitational force is about 1/300 and hence so are the dynamical oblateness and the equatorial bulge of the Earth's (geoidal) shape (e.g., Stacey & Davis, 2008; Chao, 2006, for a review).

The conventional parameter to measure the Earth's oblateness is the *oblateness coefficient* J_2 :

$$J_2 = [C - (A + B)/2]/MR^2 \quad (1)$$

where M and R denote, respectively, the Earth's mass and mean equatorial radius and $C > B > A$ are the three principal moments of inertia. J_2 is the (normalized) zonal quadrupole of the Earth's density (Chao & Gross, 1987) and related to C_{20} , the degree-2 order-0 Stokes coefficients in the spherical-harmonic expansion of the Earth's external gravitational field, by $J_2 = -\sqrt{5} C_{20}$. At 1.082636×10^{-3} , J_2 represents by far the largest deviation from a (hypothetical) spherically symmetric Earth among all Stokes coefficients. For conceptual simplicity, J_2 is often reduced to $J_2 = (C - A)/MR^2$ for an axial-symmetric Earth, thereby $A = B$.

J_2 is not constant in time; it varies in the digits beyond those quoted above, typically on the order of 10^{-10} . The zonal [degree-2, order-0] component of any mass redistribution will contribute to the time variation ΔJ_2 . Besides the seasonal water cycle in the surface geophysical fluids (atmosphere + hydrosphere + cryosphere), a host of geophysical processes cause mass redistribution on/in the Earth ranging from tides to atmosphere-ocean circulations, to denudation of glaciers/ice sheets and sea level rise, and to internal phenomena like earthquakes, glacial isostatic adjustment (GIA), and core flows.

The first evidence of ΔJ_2 was reported by Yoder et al. (1983) and Rubincam (1984), where a secular decrease of $\sim -3 \times 10^{-11}$ /year was detected from the nodal precession of the Lageos satellite by the satellite laser ranging (SLR) technique. The cause of that was attributed to the present-day phase of GIA.

Strong seasonal variabilities of J_2 , with amplitude on the order of 10^{-10} , emerged as more precise SLR monthly solutions became routine. Being seasonal, they were rightfully linked to global atmospheric mass redistributions (Chao & Au, 1991; Chao & Eanes, 1995; Cheng & Tapley, 1999; Nerem et al., 1993) and additionally the mass redistribution in land hydrology (e.g., Chao & Eanes, 1995) and presumably in the oceans and cryosphere. How well the combined meteorological contributions can “close the budget” for the observed seasonal ΔJ_2 terms is a testament to how good the meteorological models can realize the [2, 0] mass redistribution. The semiannual (and higher harmonics) ΔJ_2 terms exist not because there is actually a semiannual variability but rather because there is a mathematical artifact resulting from fitting sinusoids to the actual annual periodicity that is asymmetric in its rise-and-fall undulation due to nonlinearity in the meteorological response of the Earth system.

Knowledge was also being gained about nonseasonal characteristics of the J_2 variability. Cox and Chao (2002) reported the “1998 anomaly” when J_2 reversed its decreasing trend, an episode lasting for a few years. In search of a geophysical explanation, subsequent studies (Benjamin et al., 2006; Chao et al., 2003; Chen et al., 2003; Cheng & Tapley, 2004; Dickey et al., 2002; Meyssignac et al., 2013) illustrated the role played by the global climatic changes, seemingly related to the 1997–1998 El Niño/La Niña sequence (but see section 3.2 later). However, such effort was only partially successful owing to the then gross underestimation of oceanic variabilities by the general circulation models and the lack of observations about the cryospheric mass changes.

As more SLR data accumulated, new studies targeted the interannual ΔJ_2 anomalies (including the 1998 and other secondary anomalies) in the context of long-term variations. Benjamin et al. (2006) and Cheng et al. (2013) found remnant 18.61-year variability after the 18.61-year lunar nodal tide had been removed according to theoretical models. They also found the presence of an \sim 10-year signal of unknown origin during the three decades of observation (see also Lavallée et al., 2010).

In recent years the overall J_2 time series has significantly departed from the secular decrease and entered an upward swing rendering the long-term behavior more resembling a quadratic (parabolic) trend. The likely cause was attributed to the recent ice melting in the cryosphere (Cheng et al., 2013; Cheng & Ries, 2018; Loomis et al., 2019; Matsuo et al., 2013; Nerem & Wahr, 2011; Roy & Peltier, 2011). In particular, Loomis et al. (2019) proposed the adoption of an improved SLR J_2 series to replace that in the GRACE satellite data set. In the meantime some secondary long-term variations of J_2 were reported: (i) The earthquake-induced coseismic effects were calculated for all major earthquakes during 1976–2015 to give an average ΔJ_2 rate of -1.1×10^{-12} /year (Chao & Ding, 2016; Chao & Gross, 1987) and upward from that if including the great earthquakes circa 1960 (Xu & Chao, 2019). (ii) The Earth is becoming less oblate due to its spin down by the tidal braking at about -0.6×10^{-12} /year in ΔJ_2 rate (Chao, 2014). (iii) The impoundment of water in artificial reservoirs on land has contributed a comparable (negative) amount to the ΔJ_2 rate during the second half of the twentieth century (Chao, 2003). So together they add up to $\sim -2\text{--}3 \times 10^{-12}$ /year, constituting \sim 10% of the observed J_2 decrease. At the same time, the global sea level rise due to present-day water mass addition to the oceans at the rate of \sim 2 mm/yr (Cazenave & WCRP Global Sea Level Budget Group, 2018) should have contributed about $+3 \times 10^{-12}$ /year for J_2 (cf. Chao & O’Connor, 1988), largely nullifying the above in the long term.

The present paper revisits the nonseasonal ΔJ_2 variations on interannual-to-decadal timescales (and does not elaborate on the secular and seasonal terms as they have seen studies as described above). Seo et al. (2015) have conducted a numerical synthesis of mass redistributions in the surface geophysical fluids which were able to explain largely the interannual ΔJ_2 and again pointed to an unexplained residual \sim 10-year signal. Here we shall assess the ΔJ_2 variabilities in connection with the various interannual climatic processes in the ocean-atmosphere system, as opposed to a breakdown in terms of individual geophysical fluids (as Seo et al., 2015), following the approach delineated in Chao et al. (2003) that reported significant correlation of ΔJ_2 with the Pacific Decadal Oscillation (PDO). We shall also reinspect the 18.61-year tidal signals in ΔJ_2 , and to a lesser extent the \sim 10-year variability, in reference to theoretical models and previous studies.

2. ΔJ_2 Analysis

We first invoke the relation of the (geodetic) gravitational Stokes coefficients to the (geophysical) multipoles of Earth's density distribution ρ (e.g., Chao & Gross, 1987):

$$C_{nm} + iS_{nm} = \frac{(-1)^m 2\sqrt{(2-\delta_{m0})\pi}}{(2n+1)MR^n} \int \rho(\mathbf{r}) r^n Y_{nm}(\Omega) dV, \quad (2)$$

where M and R are, respectively, the Earth's mass and mean radius, $Y_{nm}(\Omega) = (-1)^m \left(\frac{(2n+1)(n-m)!}{4\pi(n+m)!} \right)^{\frac{1}{2}} P_{nm}(\cos\theta) \exp(im\lambda)$ is the fully normalized surface spherical harmonic of degree n order m (such that $\int Y_{n'm'}(\Omega) Y_{nm}^*(\Omega) d\Omega = \delta_{nn'} \delta_{mm'}$), P_{nm} is the associated Legendre function (in particular $P_{20} = (3\cos^2\theta - 1)/2$), and Ω is the solid angle representing colatitude θ and east longitude λ . The complex-form formulation has the strength of being more efficient for mathematical manipulation and more succinct in expressing time variations.

The change in the $[n, m]$ th Stokes coefficients can then be evaluated, to first order, by the following volume integrals:

$$\Delta C_{nm}(t) + i\Delta S_{nm}(t) = \frac{(-1)^m 2\sqrt{(2-\delta_{m0})\pi}}{(2n+1)MR^n} \int \Delta\rho(\mathbf{r}; t) r^n Y_{nm}(\Omega) dV, \quad (3)$$

in the Eulerian description (e.g., Chao et al., 1987), or

$$\Delta C_{nm}(t) + i\Delta S_{nm}(t) = \frac{(-1)^m 2\sqrt{(2-\delta_{m0})\pi}}{(2n+1)MR^n} \int \rho(\mathbf{r}) r^{n-1} \mathbf{u}(\mathbf{r}, t) \cdot [n\hat{\mathbf{r}} Y_{nm}(\Omega) + \nabla_1 Y_{nm}(\Omega)] dV, \quad (4)$$

in the Lagrangian description (Chao & Gross, 1987) where $\nabla_1 = \hat{\theta}\partial_\theta + \hat{\lambda}\csc\theta\partial_\lambda$ is the surface gradient operator. The two descriptions are equivalent to first order under the conservation of mass; the choice depends on the specific application at hand. The Eulerian approach is more convenient when the mass redistribution $\Delta\rho$ is specified, such as for the water cycle in the geophysical fluids, whereas the Lagrangian approach is used when the displacement field \mathbf{u} is available (or modeled) such as for earthquake faulting. Specifically,

$$\Delta J_2(t) = -\frac{1}{2MR^2} \int \Delta\rho(\mathbf{r}; t) r^2 (3\cos^2\theta - 1) dV, \quad (\text{Eulerian}) \quad (5)$$

$$\Delta J_2(t) = -\frac{1}{MR^2} \int \rho(\mathbf{r}) r \mathbf{u}(\mathbf{r}; t) \cdot [(3\cos^2\theta - 1) \hat{\mathbf{r}} - 3\sin\theta\cos\theta \hat{\theta}] dV. \quad (\text{Lagrangian}) \quad (6)$$

For mass transports happening on the Earth's surface, Equation 5 reduces to

$$\Delta J_2(t) = -\frac{R^2}{2M} \int \Delta\sigma(\Omega; t) (3\cos^2\theta - 1) d\Omega.. \quad (7)$$

where σ is the surface mass density. The spatial weighting (of [2,0]) is longitude-independent; hence, a purely zonal E-W mass redistribution has zero impact on J_2 . Among all latitudes, a net meridional N-S mass change happening at the poles is twice as efficient in changing J_2 as when it happens at the equator and inconsequential at the nodal latitudes of 35.3° .

We employ J_2 data available from the GRACE project, given as monthly time series for the 43-year span of 1976–2019 as Center for Space Research (CSR, University of Texas) product (courtesy of M. K. Cheng; cf. Cheng et al., 2013). The J_2 values were solved from SLR measurements to geodetic satellites, including Lageos-1, Starlette, and, since 1986, Ajisai, Lageos-2, Etalon-1 and 2, Stella, and BE-C. The 2 cm precision of modern SLR corresponds to J_2 precision within one part in 10^{11} . The theoretical values of the 18.61- and 9.3-year lunar tidal signals have been removed, so what we shall find (and report in section 4 later) with respect to the 18.61-year tide signal are the departures from the theoretical model

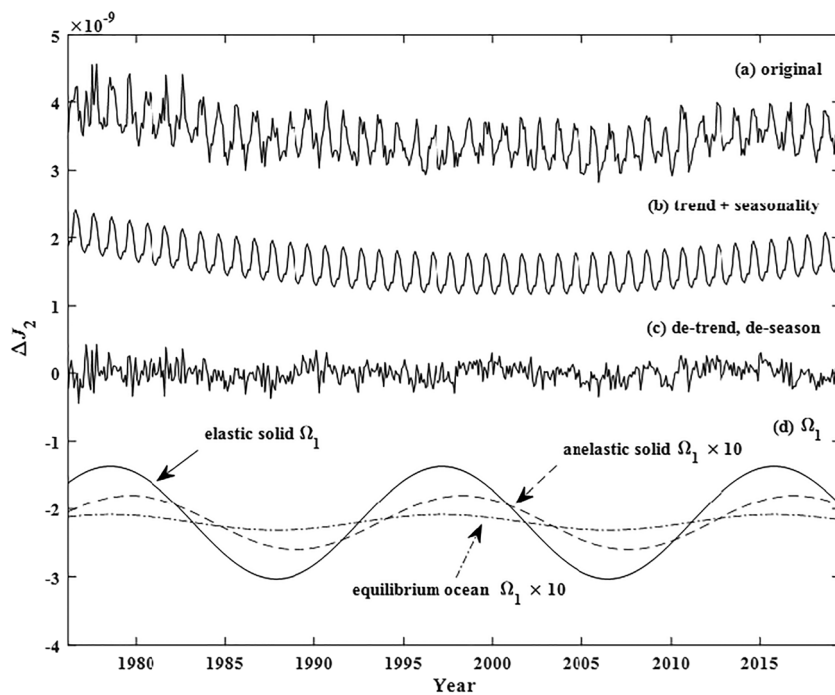


Figure 1. (a) Monthly time series of ΔJ_2 , 1976–2019. (b) The least squares fit of the quadratic trend + seasonality to (a). (c) The detrend/deseason ΔJ_2 , that is, (a) minus (b). (d) The IERS theoretical effects of the 18.61-year lunar nodal tide (Ω_1) on J_2 that were preremoved from (a), for the elastic solid tide, and the anelasticity effect and the equilibrium ocean tide (both magnified 10 times for viewing clarity). Vertical offsets for viewing clarity.

values. Also, the tidal influences on satellite orbits are accounted for when solving gravitational parameters from orbit perturbations. We have made a side inspection of another (shorter) J_2 series starting 1992 solved by the Space Research Institute (IWF) of the Austrian Academy of Sciences from the same SLR data. The two series agree well except for a minor difference in the 18.61-year signal, the origin of which is attributed to the adoption of different ocean tide models: CSR uses the CSR 4.0 model, while IWF uses the GOT 4.7 model.

Figure 1a shows the ΔJ_2 time series (1976–2019) in reference to the mean value (offset vertically for viewing clarity). The conventional Fourier power spectrum of $\Delta J_2(t)$ (after delinear, see below) in Figure 2a shows the evident annual and semiannual seasonal signals, plus some overall but barely resolved power in the low-frequency interannual-to-decadal band. The stabilized AR-z spectrum (autoregressive spectrum implemented in the complex z domain), on the other hand, proves to be more effective—it has been demonstrated (Ding & Chao, 2018) to be able to detect harmonic signals with considerably higher sensitivity and spectral resolution than the Fourier and maximum-entropy spectra. Figure 2b duplicates Ding and Chao's (2018) Figure 4, where one sees the seasonal signals from annual to higher harmonics up to five cycles per year. Appearing prominently in the longer-period band are a well-resolved 18.61-year signal along with an ~10.5-year signal. There is also a large peak at the nominal ~56 years, which evidently masquerades the aforementioned quadratic undulation of ΔJ_2 during the studied period.

Aiming at the interannual-to-decadal ΔJ_2 , we shall least squares estimate, and subsequently subtract, the secular plus the known-to-exist periodic signals from $\Delta J_2(t)$ as follows:

$$\Delta J_2(t) = (a + bt + ct^2) + \sum_i (d_i \sin \omega_i t + e_i \cos \omega_i t) + S(t), \quad (8)$$

where all coefficients a , b , c , d_i , and e_i are to be solved in a linear least squares fit by minimizing the variance of the residual S . The term detrend is to mean the subtraction of the quadratic polynomial $a + bt + ct^2$; similarly, the term delinear is to mean the subtraction of only a linear polynomial fit $a + bt$ (setting $c = 0$). In cases which will be called deseason, the periodic terms that are fit and subtracted include the annual

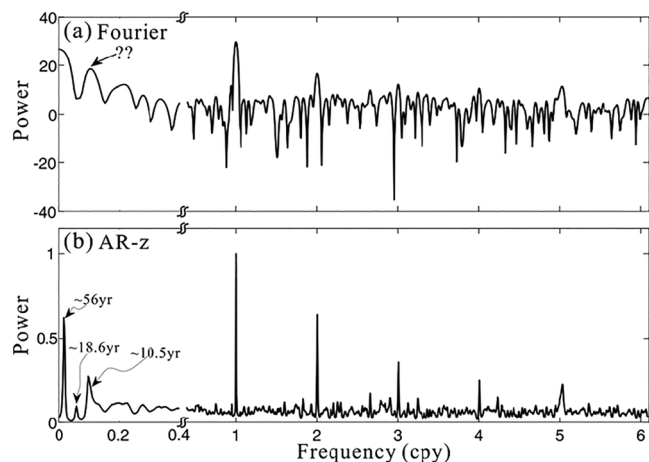


Figure 2. (a) Fourier power spectrum (on logarithmic scale) for the delinear ΔJ_2 series, 1976–2017. (b) AR-z power spectrum for the same. The long-period portion of the spectra is expanded for clarity. (Duplicated from Ding & Chao, 2018).

long-period portion of the spectra, accentuates the difficulty in resolving the interfering long-period signals. The wavelet spectra do confirm the existence of both the 10.5- and 18.61-year signals seen in the AR-z spectrum (Figure 2b). However, upon the removal of the quadratic term the apparent 18.61-year signal becomes weaker, whereas the 10.5-year signal becomes more stable in Figure 3b. We shall return to this in section 4. The nominal \sim 56-year peak in Figure 2b now masquerades as a \sim 35-year quasiperiodicity in the wavelet manifestation in Figure 3a.

term of $\omega = 2\pi/(365.25 \text{ days})$ plus corresponding semiannual, 1/3-year and 1/4-year terms. Additionally, the process of detide means if the periodic 18.61-year tidal signal is similarly fit and subtracted (applied mainly to reduce biasing influences of the tide on other components; see later).

The sum of the fitted quadratic trend + seasonality signal is shown in Figure 1b; subtracting it from Figure 1a (i.e., detrend and deseason) gives the residual shown in Figure 1c, now mainly of interannual-to-decadal timescale, to be treated below.

An effective numerical tool to elucidate possible quasiperiodic signals (cf. Chao et al., 2014), the time-frequency (Morlet) wavelet spectrum of $\Delta J_2(t)$, is presented in Figure 3 for two cases: (a) the delinear/deseason $\Delta J_2(t)$ and (b) the detrend/deseason $\Delta J_2(t)$ (i.e., Figure 1c). One sees in the interannual-to-decadal band some strong oscillations, notably one around 3–6 years, one around 10.5 years, and one at the 18.61-year tidal period (indicated by the white horizontal dashed lines).

The contrast between Figures 3a and 3b, pertaining only to the

long-period portion of the spectra, accentuates the difficulty in resolving the interfering long-period signals. The wavelet spectra do confirm the existence of both the 10.5- and 18.61-year signals seen in the AR-z spectrum (Figure 2b). However, upon the removal of the quadratic term the apparent 18.61-year signal becomes weaker, whereas the 10.5-year signal becomes more stable in Figure 3b. We shall return to this in section 4. The nominal \sim 56-year peak in Figure 2b now masquerades as a \sim 35-year quasiperiodicity in the wavelet manifestation in Figure 3a.

3. Interannual-to-Decadal ΔJ_2 : Climate Connections

3.1. Climatic Oscillations

Much of the signal power of ΔJ_2 resides in the interannual (along with intraseasonal) to decadal timescales. To better understand the origins of such variabilities, we now search for causal links of various climatic oscillations in the atmosphere-ocean system to ΔJ_2 by examining the (cross-)correlation functions and the corresponding (cross-)coherence spectra among them.

Figure 4a is the detrend, deseason, detide $\Delta J_2(t)$ obtained as above; Figures 4b–4f respectively are the monthly time series of indices of PDO, Antarctic Oscillation (AAO), Arctic Oscillation (AO), El Niño–Southern Oscillation (ENSO), and Atlantic Multidecadal Oscillation (AMO). A climatic oscillation index is a nondimensional function of time derived from relevant meteorological observations; its values indicate the polarity and strength of the oscillation in question at the given epoch. The index amplitudes are here further normalized with respect to their respective standard deviation (for the benefit of fitting for Equation 9 later).

The PDO Index is defined as the leading principal component of the monthly mean sea surface temperature variability over the North Pacific sector poleward of 20°N . The AAO describes the intensity of westerly wind belt surrounding the Antarctic, quantified by the AAO Index (data unavailable before 1979, for which we zero-pad) which is the leading principal component of the 700 hPa atmospheric geopotential height anomalies poleward of 20°S . The AO is to be interpreted as the surface signature of modulations in the strength of the polar vortex aloft the Arctic (Thompson & Wallace, 2000), while the AO Index is constructed by projecting the 1,000 hPa height anomalies poleward of 20°N . The ENSO is the strong recurring climate pattern involving changes in the temperature of seawater and air pressure in the tropical Pacific Ocean; the Multivariate ENSO Index (MEI) used here is the first principal component of five main observed climatic variables over the tropical Pacific. The AMO is a coherent mode of natural variability based upon the average anomalies of sea surface temperatures, with AMO Index to reflect the nonsecular multidecadal sea surface temperature pattern variability in the North Atlantic basin.

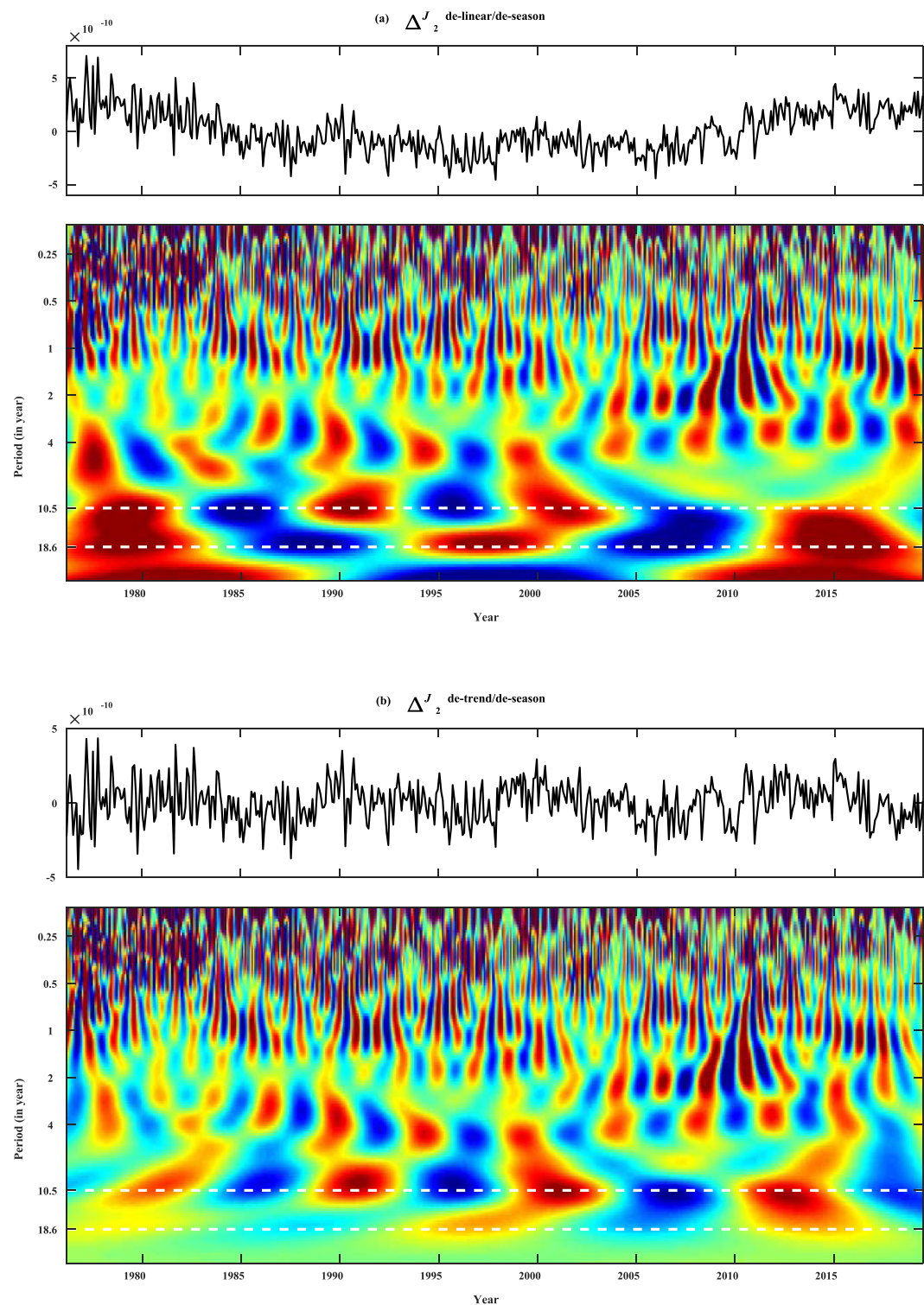


Figure 3. Time series and the Morlet wavelet time-frequency spectrum of (a) the delinear/deseason $J_2(t)$ and (b) the detrend/deseason $\Delta J_2(t)$. Red color indicates peak values, and blue trough values. The white dashed lines indicate the 10.5- and 18.61-year periodicities.

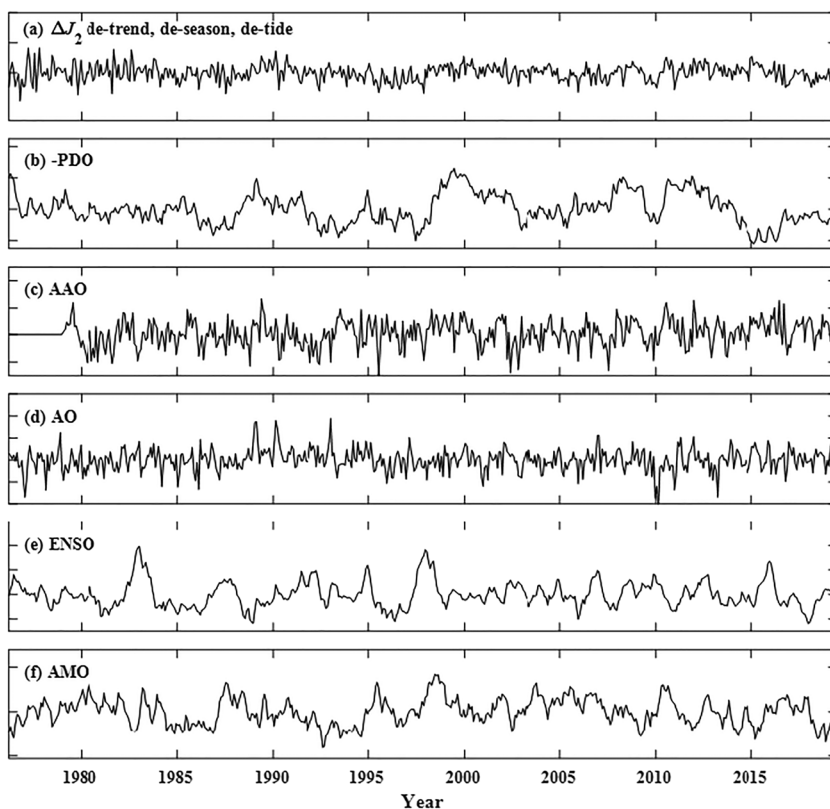


Figure 4. Time series in this study: (a) The detrend/deseason/detide $\Delta J_2(t)$. (b–f) The indices of, respectively, Pacific Decadal Oscillation (PDO, rotated, and polarity reversed), Antarctic Oscillation (AAO; data unavailable before 1979), Arctic Oscillation (AO), El Niño–Southern Oscillation (ENSO, rotated), and Atlantic Multidecadal Oscillation (AMO). All amplitudes are normalized with respect to standard deviation.

Despite the difference in their primary timescales, PDO and ENSO carry considerable correlation between their conventional indices because of their geographical juxtaposition in the Pacific thus sharing commonality in their physical behavior. That makes identifying their individual contributions to ΔJ_2 troublesome. Therefore, in this paper we adopt the slightly modified PDO and ENSO Indices that are designed to be orthogonal to each other during the studied period as obtained by Chen and Wallace (2016) via rotated principal component. In effect this dissociates the long-period portion of the ENSO power and merges it into PDO.

3.2. Correlation Functions and Coherence Spectra

Figure 5 gives the correlation function of (the detrend/deseason/detide) ΔJ_2 with respect to the five climatic oscillations of Figure 4 as a function of relative time shift (where positive time shift means ΔJ_2 leading). We further calculate the (complex) coherence spectrum in the frequency domain to delineate how each correlation breaks down according to timescale.

Figure 6 presents the coherence magnitude squared and coherence phase as functions of frequency (in logarithmic scale and labeled in period so as to accentuate the long-period portions). Here we adopt the calculation algorithm and the corresponding confidence levels from Chao and Eanes (1995; see also Chao & Chung, 2019), where seven orthogonal multitapers (Thomson, 1982) with time bandwidth product of 4π are employed to evaluate the spectral-averaged cross- and auto-Fourier spectra in the process of calculating the coherence. Figure 6a is the coherence spectrum of ΔJ_2 with respect to PDO, AAO, and AO, the three climatic oscillations that are found to correlate with ΔJ_2 (Figure 5). Figure 6b is the same as Figure 6a except that the ΔJ_2 time series has further undergone a “de-atmosphere” procedure, whereof the atmospheric effect on ΔJ_2 is calculated according to Equation 7 followed by subtraction. The calculation uses the National Centers for Environmental Prediction (NCEP) monthly mean surface pressure reanalysis data, including

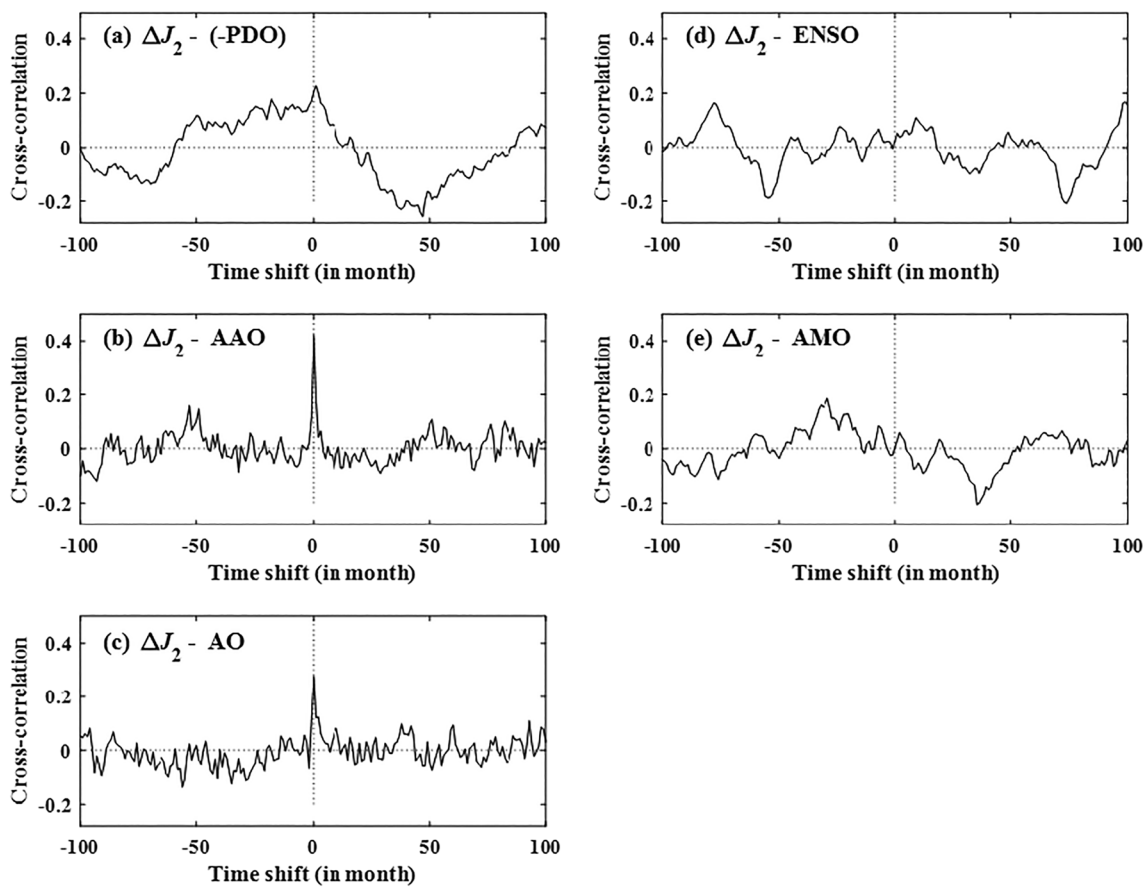


Figure 5. (a–e) The correlation function of the detrend/deseason/detide ΔJ_2 with respect to the five climatic oscillations of Figure 4 as a function of relative time shift (where positive time shift means ΔJ_2 leading).

the inverted-barometer correction (e.g., Wunsch & Stammer, 1997). The purpose of de-atmosphere procedure is to unravel the atmospheric contribution from other contributions to ΔJ_2 .

Figures 5d and 5e pronounce virtually null correlation of ΔJ_2 with ENSO and AMO. The absence of correlation between ΔJ_2 and AMO apparently reflects AMO's dominantly thermal effect than net mass transport and the fact that the AMO timescale is generically more disparate (longer) than that of ΔJ_2 . The absence of ENSO signature in ΔJ_2 , contrary to that alluded to in Cheng and Ries (2018), corroborates the notion that ENSO, although a major climatic influence, involves mostly E-W zonal variability (in the tropical Pacific) as far as mass transport is concerned and hence is ineffective in causing ΔJ_2 . The latter also appears to be consistent with the finding of Adhikari and Ivins (2016) of the strong variabilities in the tesseral [2, 1] component that oscillates E-W within the zonal band of 30–50° north and south. We have in addition examined the ENSO effect in two separate types (Yu & Kao, 2007), namely, the east Pacific type that dominated in the 20th century and the Central Pacific type that prevailed in the 21st century, in terms of their corresponding indices (from <https://www.ess.uci.edu/~yu/2OSC/>). We find no correlation of either with ΔJ_2 (not shown here). In that regard, it is worth to point out that the excess precipitation on land during the 2011 central Pacific-type La Niña that was found to lower the global mean sea level (Boening et al., 2012) left no appreciable signature in ΔJ_2 .

Figures 5b and 5c, on the other hand, clearly show that ΔJ_2 correlates well with both AAO and AO with virtually zero time shift implying instant response to the forcing at monthly resolution. Their respective correlation coefficients, 0.42 and 0.28, are well above the 99% confidence level on account of the degree of freedom associated with the broadband data sets here (e.g., Chao & Chung, 2019). Figure 6a further shows that the correlation between ΔJ_2 and AO concentrates in the period band of 3–6 years, whereas that between ΔJ_2

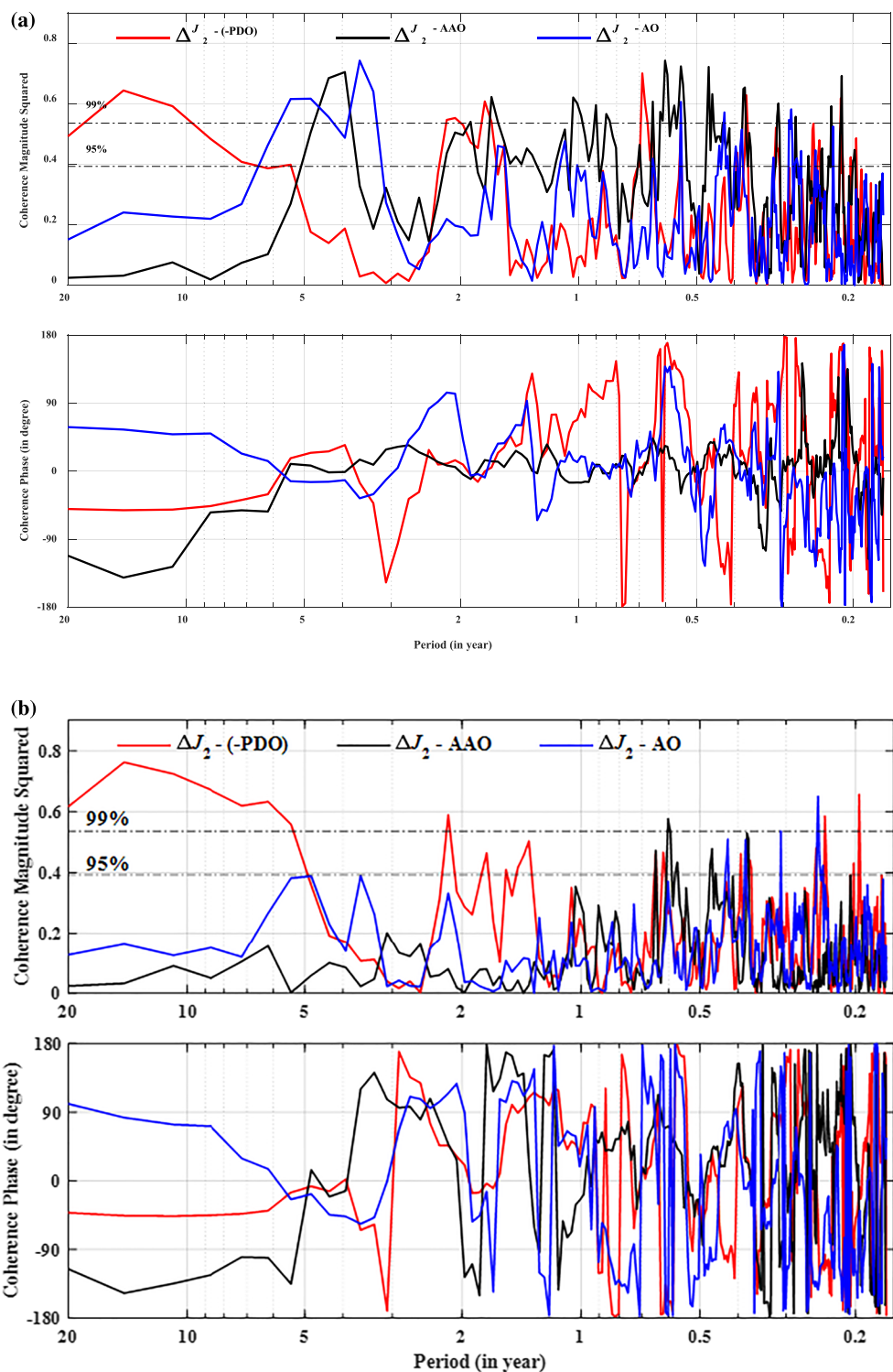


Figure 6. Coherence spectra in terms of magnitude squared and phase (whereof positive phase means ΔJ_2 leading) as functions of period. (a) For detrend/deseason/detide ΔJ_2 with respect to PDO (polarity reversed), AAO, and AO. (b) Same as (a) but for ΔJ_2 after further de-atmosphere procedure.

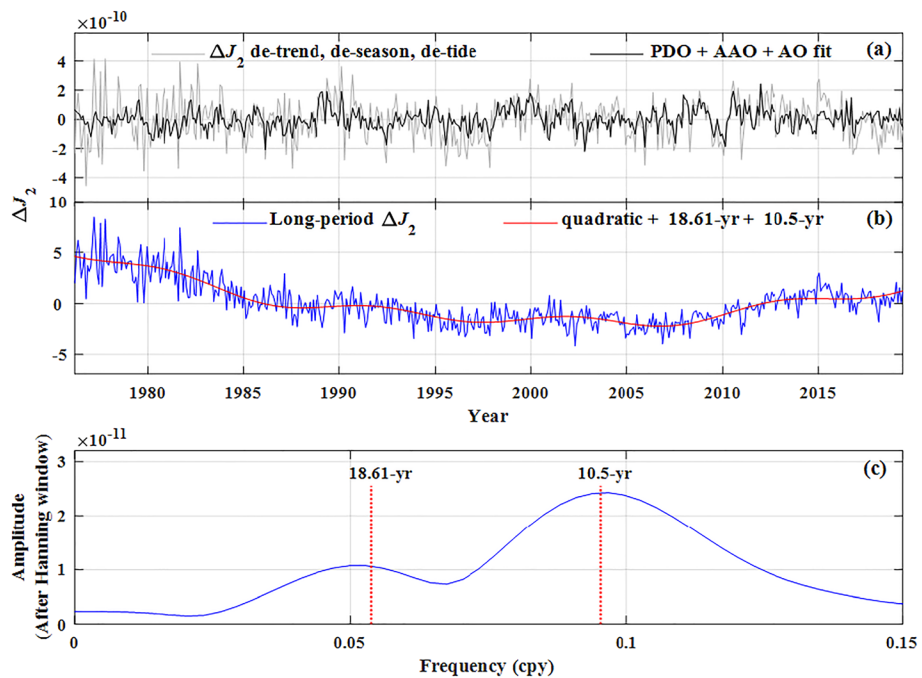


Figure 7. (a) Comparison of the detrend/deseason/detide ΔJ_2 with the least squares fit $k_{\text{PDO}} \cdot \text{PDO}(t) + k_{\text{AAO}} \cdot \text{AAO}(t) + k_{\text{AO}} \cdot \text{AO}(t)$. (b) the deseason ΔJ_2 minus $k_{\text{PDO}} \cdot \text{PDO}(t) + k_{\text{AAO}} \cdot \text{AAO}(t) + k_{\text{AO}} \cdot \text{AO}(t)$, with the overlaid least squares fit of quadratic +18.61-year +10.5-year terms. (c) the Hanning-windowed Fourier amplitude spectrum of (b) minus the quadratic term.

and AAO is more broadband ranging from (the intraseasonal) several months to about 5 years. Throughout these ranges the coherence phases are found to be near 0 confirming the finding above. In particular, the 3- to 6-year quasiperiodicity of ΔJ_2 seen in the wavelet spectrum Figure 8 is evidently a conspired sum effect of AAO and AO.

The Southern Hemisphere AAO (also known as the Southern Annular Mode) is characterized by a circumpolar belt of westerly wind circulation entrapping the polar high-pressure frigid air. As dictated by Equation 7, the largely zonal AAO by itself is ineffective in changing J_2 ; what is duly captured in ΔJ_2 is its associated N-S meridional mass migration. During the positive phase of the AAO Index, the westerly wind intensifies and the belt contracts poleward, increasing J_2 in the process, as evidenced in their correlation in Figures 5b and 6a. During the negative phase the reverse occurs, where the westerly weakens letting the polar air breach into lower latitudes, decreasing J_2 .

Counterpart to AAO, the Northern Hemisphere AO (also known as the Northern Annular Mode) behaves in a similar way, influencing ΔJ_2 and resulting in the similar correlation with ΔJ_2 . An example of the AO episode is the series of historic snowstorms in North America in early 2010 when the frigid polar air breached out during the strong negative phase of the AO Index.

On the other hand, comparing Figure 6b with 6a makes it evident that the high coherences of ΔJ_2 with AAO and AO above are eliminated entirely by the de-atmosphere procedure. That implies that it is the atmospheric mass transports associated with AAO and AO that are responsible for the intraseasonal to interannual (nonseasonal) ΔJ_2 variability, leaving little or at most secondary contributions from the oceans and land hydrology. For example, although the variation in oceanic mass transport of the Antarctic Circumpolar Current is highly correlated with AAO (Liau & Chao, 2017), that apparently only contributed negligibly to ΔJ_2 presumably because of its dominantly zonal nature.

Chao et al. (2003) has demonstrated a clear correlation between ΔJ_2 and $-\text{PDO}$ (the sign of PDO there is the opposite to the sign here). In particular, note that although the large 1998 J_2 anomaly appears to have onset near contemporary with the 1987–88 El Niño event, its far longer duration of ~5 years in fact corresponds

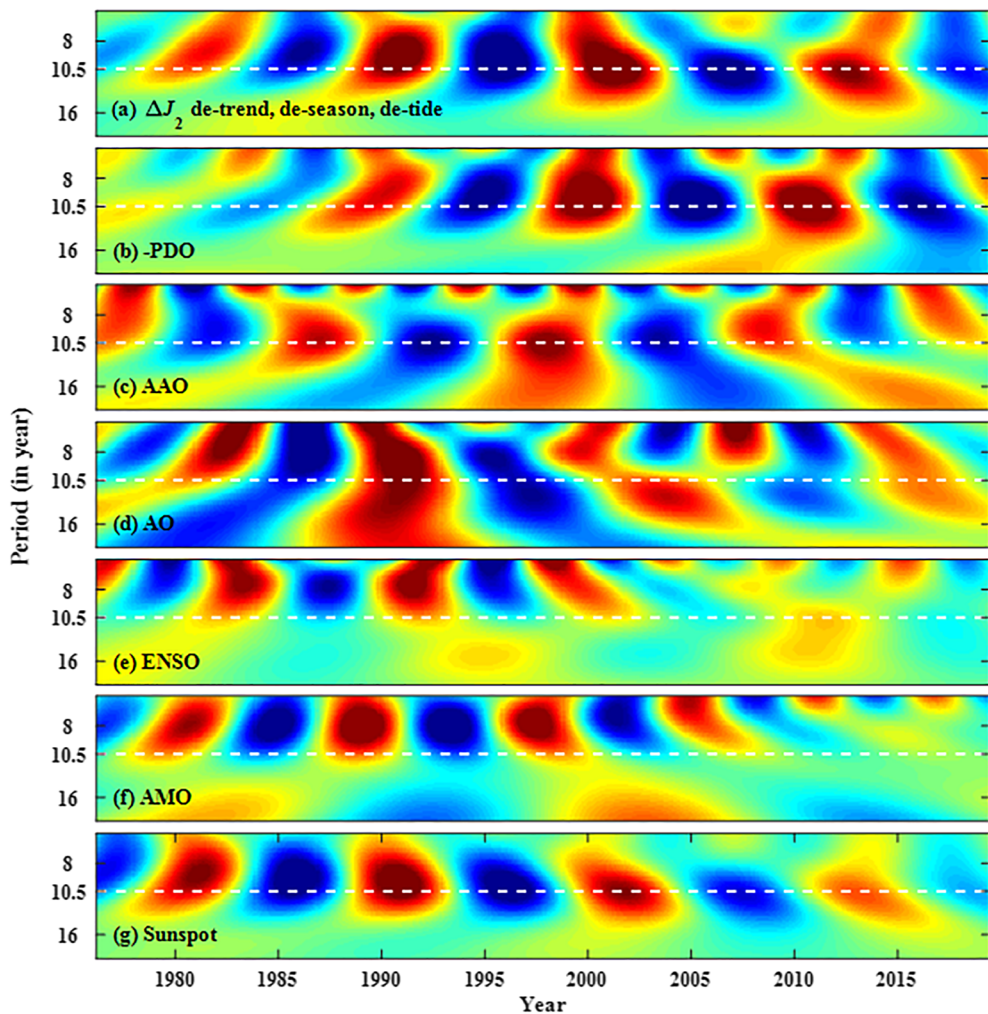


Figure 8. The Morlet wavelet spectra in the decadal band around the 10.5-year period (indicated by the white dashed lines) for (a) detrend/deseason/detide ΔJ_2 . (b–f) Respectively the indices (see Figure 4) of Pacific Decadal Oscillation (PDO, with polarity reversed), Antarctic Oscillation (AAO), Arctic Oscillation (AO), El Niño–Southern Oscillation (ENSO), and Atlantic Multidecadal Oscillation (AMO). (g) the (de-mean) sunspot variation. Red indicates positive peak, and blue negative peak.

well with PDO (see Figure 12 of Chao et al., 2003), not with ENSO, as further corroborated here. Figure 5a shows a correlation of 0.23 between ΔJ_2 and –PDO, at the nominal ΔJ_2 time lead of 1 month which is also indicated in the coherence phase in Figure 6. The correlation peak is broad because of the long-period characteristic of PDO; the apparent ~10-year undulation with respect to the time shift implies the strong presence of such periodicity in both PDO and ΔJ_2 . Figure 6 reveals that this correlation resides in two period bands: around ~2 years and longer than ~5 years. The former, at near-zero phase, gets reduced partially by the de-atmosphere procedure (Figure 6b) and hence is attributable to the combination of the atmospheric and the oceanic mass redistributions. The coherence at timescales longer than ~5 years on the other hand becomes even more prominent after the de-atmosphere procedure, implying that the main contribution of PDO to ΔJ_2 on such timescale is the N–S water mass transport in the ocean, in contrast to AAO and AO.

3.3. Fitting ΔJ_2 With the Climatic Oscillations

It is appropriate at this point to estimate the individual contributions of AAO, AO, and PDO to ΔJ_2 in absolute quantity. We thus incorporate into Equation 8 the additional respective terms:

$$\Delta J_2(t) = (a + bt + ct^2) + \sum_i (d_i \sin \omega_i t + e_i \cos \omega_i t) + k_{\text{PDO}} * \text{PDO}(t) + k_{\text{AAO}} * \text{AAO}(t) + k_{\text{AO}} * \text{AO}(t) + S_1(t), \quad (9)$$

on which (where the periodic terms include only the seasonality) we perform a new least squares regression by minimizing the variance of the residual S_1 . The least squares estimated admittance coefficients k can potentially provide integrative constraints on the quantitative modeling of these climatic oscillations. Here the PDO Index is time shifted by 1 month on account of our finding above, and the fit time span is somewhat shorter because the AAO Index series did not start until 1979 (cf. Figure 4). The results are the following: k_{PDO} amounts to -2.26×10^{-11} of ΔJ_2 per unity PDO Index, k_{AAO} to $+5.66 \times 10^{-11}$ of ΔJ_2 per unity AAO Index, and k_{AO} to $+3.12 \times 10^{-11}$ of ΔJ_2 per unity AO Index. These numbers when normalized by their respective standard deviations become $k_{\text{PDO}} = -2.17 \times 10^{-11}$, $k_{\text{AAO}} = +5.41 \times 10^{-11}$, and $k_{\text{AO}} = +3.17 \times 10^{-11}$, which thus indicate the relative importance of each oscillation in contributing to ΔJ_2 .

A comparison of the detrend/deseason/detide ΔJ_2 with the least squares fit $k_{\text{PDO}} * \text{PDO}(t) + k_{\text{AAO}} * \text{AAO}(t) + k_{\text{AO}} * \text{AO}(t)$ is presented in Figure 7a, not surprisingly showing a good match. Here we report that the standard deviation of the detrend/deseason/detide ΔJ_2 is 13.5×10^{-11} , while that after the removal of the fit $k_{\text{PDO}} * \text{PDO}(t) + k_{\text{AAO}} * \text{AAO}(t) + k_{\text{AO}} * \text{AO}(t)$ is significantly reduced to 8.5×10^{-11} .

4. The ~10.5-Year Variability and the 18.61-Year Ω_1 Tidal Signal

With our optimum estimates of the admittances of the climatic oscillations PDO, AAO, and AO in Equation 9, we now go back to the original ΔJ_2 series, from which we remove these oscillations as well as the seasonal terms. The result, that is, $S_1(t)$ in Equation 9, is presented in Figure 7b, which is considered to be a “clean” long-period $\Delta J_2(t)$ in order to examine the decadal and longer variabilities of presumably non-climatic origin, or symbolically: Long-period $\Delta J_2(t) = \text{Quadratic polynomial} + 10.5\text{-year sinusoids} + 18.61\text{-year sinusoids}$. The least squares fit of these three terms is overlaid in Figure 7b.

The Hanning-windowed Fourier spectrum of the long-period $\Delta J_2(t)$ minus the quadratic trend is shown in Figure 7c, with spectral amplitude numerically scaled with synthetic calibration. The vertical lines show the prominent presence of two resolved long-period signals which are not resolvable in Figure 2a, one of 10.5 years at half-amplitude $\sim 4.8 \times 10^{-11}$, and one of 18.61 years at half-amplitude $\sim 2.1 \times 10^{-11}$.

Focusing on the decadal variabilities in the period band around 10.5 years, Figure 8 presents a closer examination of the wavelet spectra among all the above data series. The wavelet spectra of ΔJ_2 and –PDO do manifest strong correspondence consistent with the above. There also appears to be some power in AAO at ~ 10 years but uncorrelated with ΔJ_2 as evident in Figure 6. The other climatic oscillations, AO, ENSO and AMO, all lack power at this timescale.

In Figure 8g we plot the wavelet spectrum of the sunspot variation (after de-mean) with its well-known 11-year periodicity. This 11-year solar cycle over the studied time span apparently corresponds well in phase to the ~ 10.5 -year ΔJ_2 . Suggestion of a causal relationship between climatic fluctuation and the solar cycle has long been a matter of debate; that in the present case of ΔJ_2 has been noted by Seo et al. (2015) and Cheng and Ries (2018). We will refrain from making speculations here in the absence of plausible causal mechanisms and without further study that is beyond the present scope. On the other hand, it is possible that the apparent correlation comes from artifact error in the modeling of solar radiation influences on the SLR satellite orbits, including solar pressure, the Yarkovsky-Schach thermal effect, and charged particle drag (cf. Métris et al., 1997; Rubincam, 1990). These artifacts can lead to apparent solar cycle signatures that have not been calibrated and corrected out in the solution of ΔJ_2 and cannot be ruled out at this time.

The 18.61-year tide (termed Ω_1 per IERS Convention 2010) due to the lunar orbit nodal precession is known to affect J_2 greatly given its zonal $[2, 0]$ spatial pattern. The higher harmonic tide Ω_2 at period of 9.3 years is ~ 100 times smaller and here neglected. The theoretical Ω_1 terms are displayed in Figure 1d according to the IERS Convention 2010 (Petit & Luzum, 2010). They include three effects on ΔJ_2 , respectively due to (i) the dominant solid tide of the elastic Earth, (ii) the modification of (i) owing to the mantle anelasticity, and (iii) the ocean tide that is assumed to be of equilibrium.

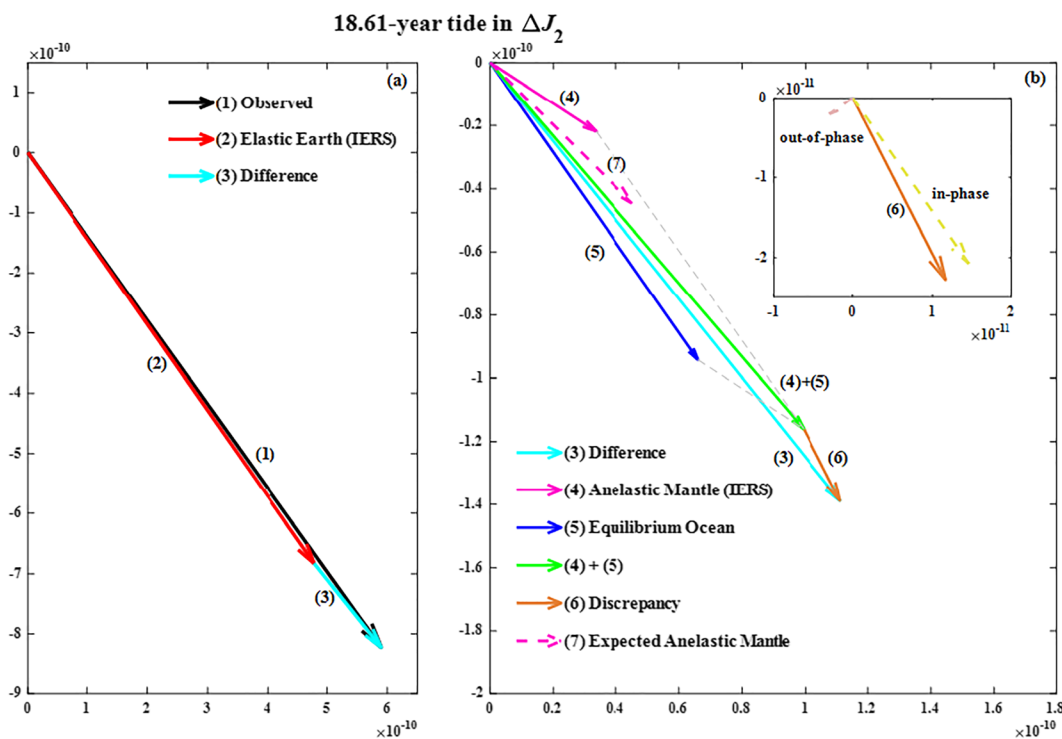


Figure 9. Phasor diagram of the 18.61-year Ω_1 tidal terms in ΔJ_2 . (a) Phasor (3) = (1) – (2) is the difference of the “true” observed from the IERS theoretical solid tide model, transplanted to the zoom-in of (b). (b) Phasor (6) = (3) – [(4) + (5)] is the discrepancy of (3) from the IERS theoretical models of mantle anelasticity + equilibrium ocean tide. The in-phase/out-of-phase decomposition of Phasor (6) is given in the inset. Phasor (7) is the anelastic mantle expected from observation (1).

Specifically, (i) is obtained through a direct conversion from the tidal potential via the Love number $k_2 = 0.30190$; the (peak) half amplitude (at the poles) is 2.793 cm. (Note that the IERS Convention 2010’s tide table in ftp://tai.bipm.org/iers/conv2010/chapter6/tidemodels/fes2004_Cnm-Snm.dat associated with its Equation (6.15) has an error—the unit should be 10^{-11} , not 10^{-12}). Effect (ii) is obtained similarly but via the additional $\delta k_2 = 0.01347 - 0.00541i$, the imaginary part stemming from the anelasticity consistent with the model of Wahr and Bergen (1986), which introduces a small phase lag off equilibrium based on the selected reference period of 200 s and power law index of 0.15. Effect (iii), being equilibrium and hence synchronous in phase with (i), is calculated by integration of the Ω_1 potential over the oceanic area and multiplied by the factor $(1 + k_2 - h_2)(1 + k'_2) = 0.476$, where $k_2 = 0.29525$ and $h_2 = 0.6078$ are, respectively, the gravimetric and vertical geometric Love numbers, and the gravimetric load Love number $k'_2 = -0.3075$ is to account for the elastic deformation of the solid Earth under the additional ocean water mass loading. The normalized amplitude used in the CSR J_2 series for Ω_1 equilibrium ocean tide is 0.4224 cm.

Thus, we undo the removal of these theoretical terms by adding them back to ΔJ_2 . A least squares fit in the same form as before (the inclusion of the 10.5-year terms is to absorb empirically the 10.5-year power to mitigate the interference with Ω_1) then gives rise to the following estimates for Ω_1 that we summarize in the phasor diagrams (cf. Melchior, 1989) of Figure 9.

The (black) Phasor (1) in Figure 9a gives our estimate of the Ω_1 tidal amplitude in the “true” ΔJ_2 (where the theoretical Ω_1 terms are restored), which in the polar form is $(1.01 \times 10^{-9}, -54^\circ)$ with the phase referenced to epoch 2000.0 as defined in the IERS Convention. The (red) Phasor (2) is the IERS theoretical solid tide effect (i) above. Their difference, the (light blue) Phasor (3) = (1) – (2) transplanted to the zoom-in of Figure 9b, is therefore to be attributed to the two physical effects (ii) and (iii) above.

Now in Figure 9b the sum of Phasor (4), the IERS theoretical mantle anelasticity effect (ii), and Phasor (5), the theoretical equilibrium ocean effect (iii) (per M. K. Cheng; see above), indeed accounts for the bulk of the “observed” Phasor (3), but not completely—we are left with a discrepancy (orange) Phasor

(6) = (3) – [(4) + (5)] = $(2.56 \times 10^{-11}, -63^\circ)$. Within our estimation uncertainties (see below), Phasor (6) thus signifies the part of Ω_1 signal in ΔJ_2 that is missed by either or a combination of the theoretical models for effects (ii) and (iii). We can decompose it into the in-phase component (along the tidal potential itself) and the out-of-phase component, as in the inset of Figure 9b. The in-phase component, being dominant, calls for an augmentation in value for the mantle anelasticity's in-phase effect or the equilibrium ocean tide Ω_1 model or a combination of the two. Similarly, the smaller out-of-phase component calls for a reduction in phase delay, and hence energy dissipation, from what is theoretically believed for the mantle anelasticity (per model of Wahr & Bergen, 1986) plus some slight off equilibrium of the ocean Ω_1 tide. Presently there is no compelling evidence for the latter, although small differences in numerics exist among self-consistent models due to model grid resolution in computation even assuming equilibrium (cf. Agnew & Farrell, 1978; Woodworth, 2012). Thus, attributing Phasor (6) solely to mantle anelasticity would mean its net value should be Phasor (7) instead of (4), with about twice the in-phase component and about half of the phase delay as (4).

The above arguments in principle point to possible quantitative improvements of the present theoretical models. However, here we shall not pursue so for the following reason. In principle, a \sqrt{N} processing gain (N being the number of independent data points) in the estimation of a single-frequency signal (here the Ω_1 tidal term in ΔJ_2) renders, in our case, a nominal reduction of the uncertainty to $\sim 10^{-11}/20 \sim 0.5 \times 10^{-12}$ or a few times higher for earlier years, which is comfortably smaller than, say, the discrepancy Phasor (6) or the Ω_1 tide amplitude. However, that is the formal error due to random noises, whereas here one faces systematic errors in the form of interferences from the spectral neighbors during the present time span, in our case those modeled nominally as a 10.5-year sinusoid and a quadratic polynomial (cf. Figure 3). Presently lacking full knowledge of these interfering signals, it is not very meaningful to draw quantitative inferences but to await future, longer data to afford better spectral resolutions.

5. Concluding Remarks

ΔJ_2 contains a broad band of signals due to a host of physical processes that involve large-scale N-S mass redistributions in the Earth. In this study we analyze these signals in the SLR-observed ΔJ_2 data series for 43 years of 1976–2019. We first remove numerically the well-observed quasi-quadratic variation during this period due to GIA and the accelerating land ice melting, and the well-studied seasonal terms due to seasonality of the surface geophysical fluids. We then examine the interannual-to-decadal ΔJ_2 in its correlations with various climate oscillations of the atmosphere-ocean system in terms of their respective indices. We are able to elucidate and discern the contributions of AAO and AO (for timescale shorter than 5 years), PDO (for timescale longer than 5 years), and the absence thereof in ENSO and AMO.

Ensuing least squares fit allows the estimation and the removal of their contributions from ΔJ_2 , revealing two remaining, nonclimatic long-period signals: (1) A ~ 10.5 -year signal is found to be tantalizingly correlated with the solar cycle; this correlation may originate from errors in the modeling of solar radiation (cf. Métris et al., 1997; Rubincam, 1990) but is uncertain presently. (2) For the 18.61-year Ω_1 tidal signal in ΔJ_2 , our estimates in comparison to the theoretical models (per IERS) calls for an approximately twofold augmentation in the in-phase value and a reduction by half of the out-of-phase value over the theoretical model values, enabling further quantitative inferences for the models. But we choose to defer such studies because of the lack of knowledge about systematic errors due to spectral interferences in our numerical estimates.

The detrend/deseason/detide ΔJ_2 series in Figure 4a has a standard deviation of 13.5×10^{-11} . With all the known or modeled signals considered and least squares estimated above, the standard deviation for the residual (i.e., the difference between the two curves in Figure 7a) is significantly reduced to 8.5×10^{-11} . What geophysical signals are still remaining in this ΔJ_2 “final” residual? For example, mass redistributions that occur in the Earth's cores driven by geodynamo actions (cf. Kuang et al., 2017) can have nonvanishing [2,0] component and contribute to ΔJ_2 , although Equations 5 and 6 dictate lower sensitivity to the observed excursions in ΔJ_2 detected by SLR as the radial distance to the source gets larger. Note, however, the rotational normal modes including the free-core nutation, inner-core wobble (e.g., Mathews et al., 2002), and

inner-core axial libration (Chao, 2017) to first order contain no [2,0] component in the associated mass variation.

In another example, we have compared the final residual ΔJ_2 with the ΔJ_2 caused cumulatively by coseismic mass dislocation due to the 22 largest earthquakes in the 21st century. The latter is calculated as in Xu and Chao (2019). The cumulative effect over time (figure not shown) shows a secular decrease in ΔJ_2 , as reported in Chao and Gross (1987) and Chao and Ding (2016), and has a standard deviation of 6.4×10^{-11} , comparable to that of the ΔJ_2 final residual and, as such, indicating its potential importance. However, no correspondence is evident between the two time series as would be anticipated. Besides the relatively high noises and the remaining contaminations from other sources, one possible major reason is that the cumulative coseismic effect may have been removed numerically at the outset by the quadratic polynomial fit to ΔJ_2 that we have performed. Furthermore, postseismic variations can be comparable to, if not larger than, and augment the coseismic effects, as suggested by, for example, Adhikari et al. (2018) and Xu and Chao (2019). Such fine and detailed signals await further studies.

Acknowledgments

Thanks are due to the following organizations that provide the data sets used in this paper: J_2 from the Center for Space Research at the University of Texas, Austin (<https://grace.jpl.nasa.gov/data/get-data/oblateness/>); the auxiliary J_2 from the Space Research Institute (IWF) of the Austrian Academy of Sciences (http://geodesy.iwf.ac.at/d_slr_monthly.html); the monthly AAO and AO indices and the surface pressure from NCEP (http://www.cpc.ncep.noaa.gov/products/precip/CWlink/daily_ao_index/ao/monthly.ao.index.b79.current.ascii; http://www.cpc.ncep.noaa.gov/products/precip/CWlink/daily_ao_index/monthly.ao.index.b50.current.ascii); [https://www.esrl.noaa.gov/psd/data/gridded/data.ncep.reanalysis.surface.html](http://www.esrl.noaa.gov/psd/data/gridded/data.ncep.reanalysis.surface.html); and AMO index (from [https://www.esrl.noaa.gov/psd/data/correlation/amon.us.long.data](http://www.esrl.noaa.gov/psd/data/correlation/amon.us.long.data)); the orthogonal version of the ENSO and PDO indices were graciously provided by Xianyao Chen. We also thank E. Ivins for an insightful and careful review, and C. Y. Xu for assistance. This work is supported by Taiwan Ministry of Science and Technology Grant 108-2116-M-001-016.

References

- Adhikari, S., Caron, L., Steinberger, B., Reager, J. T., Kjeldsen, K. K., Marzeion, B., et al. (2018). What drives 20th century polar motion? *Earth Planetary Science Letters*, 502, 126–132. <https://doi.org/10.1016/j.epsl.2018.08.059>
- Adhikari, S. L., & Ivins, E. R. (2016). Climate-driven polar motion: 2003–2015. *Science Advances*, 2(4), e1501693. <https://doi.org/10.1126/sciadv.1501693>
- Agnew, D. C., & Farrell, W. E. (1978). Self-consistent equilibrium ocean tides. *Geophysical Journal of the Royal Astronomical Society*, 55(1), 171–181. <https://doi.org/10.1111/j.1365-246X.1978.tb04755.x>
- Benjamin, D., Wahr, J., Ray, R. D., Egbert, G. D., & Desai, S. D. (2006). Constraints on mantle anelasticity from geodetic observations, and implications for the J_2 anomaly. *Geophysical Journal International*, 165(1), 3–16. <https://doi.org/10.1111/j.1365-246X.2006.02915.x>
- Boening, C., Willis, J. K., Landerer, F. W., Nerem, R. S., & Fusillo, J. (2012). The 2011 La Niña: So strong, the oceans fell. *Geophysical Research Letters*, 39, L19602. <https://doi.org/10.1029/2012GL053055>
- Cazenave, A., & WCRP Global Sea Level Budget Group (2018). Global sea-level budget 1993–present. *Earth System Science Data*, 10, 1551–1590. <https://doi.org/10.5194/essd-10-1551-2018>
- Chandrasekhar, S. (1933). The equilibrium of distorted polytropes, I: The rotational problem. *Monthly Notices of the Royal Astronomical Society*, 93(5), 390–406. <https://doi.org/10.1093/mnras/93.5.390>
- Chao, B. F. (2004). Geodesy is not just for static measurements any more. *Eos, Transactions American Geophysical Union*, 84, 145–156.
- Chao, B. F. (2006). Earth's oblateness and its temporal variations. *Comptes rendus Geoscience*, 338(14–15), 1123–1129. <https://doi.org/10.1016/j.crte.2006.09.014>
- Chao, B. F. (2014). On gravitational energy associated with the Earth's changing oblateness. *Geophysical Journal International*, 199(2), 800–804. <https://doi.org/10.1093/gji/ggu301>
- Chao, B. F. (2017). Dynamics of axial torsional libration under the mantle–inner core gravitational interaction. *Journal of Geophysical Research*, 121. <https://doi.org/10.1002/2016JB013515>
- Chao, B. F., & Au, A. Y. (1991). Temporal variation of Earth's zonal gravitational field caused by atmospheric mass redistribution: 1980–1988. *Journal of Geophysical Research*, 96(B4), 6569–6575. <https://doi.org/10.1029/91JB00042>
- Chao, B. F., Au, A. Y., Boy, J.-P., & Cox, C. (2003). Time-variable gravity signal of an anomalous redistribution of water mass in extratropic Pacific during 1998–2002. *Geochemistry Geophysics Geosystems*, 4, 1096. <https://doi.org/10.1029/2003GC00589>
- Chao, B. F., & Chung, C. H. (2019). On estimating the cross-correlation and least-squares fit of one dataset to another with time shift. *Earth Space Science*, 6(8), 1409–1415. <https://doi.org/10.1029/2018EA000548>
- Chao, B. F., Chung, W. Y., Shih, Z. R., & Hsieh, Y. K. (2014). Earth's rotation variations: A wavelet analysis. *Terra Nova*, 26(4), 260–264. <https://doi.org/10.1111/ter.12094>
- Chao, B. F., & Ding, H. (2016). Global coseismic geodynamic changes induced by all major earthquakes, 1976–2015. *Journal of Geophysical Research*, 121, 8987–8999. <https://doi.org/10.1002/2016JB013161>
- Chao, B. F., & Eanes, R. J. (1995). Global gravitational change due to atmospheric mass redistribution as observed by the Lageos' nodal residual. *Geophysical Journal International*, 122(3), 755–764. <https://doi.org/10.1111/j.1365-246X.1995.tb06834.x>
- Chao, B. F., & Gross, R. S. (1987). Changes in the Earth's rotation and low-degree gravitational field induced by earthquakes. *Geophysical Journal of the Royal Astronomical Society*, 91(3), 569–596. <https://doi.org/10.1111/j.1365-246X.1987.tb01659.x>
- Chao, B. F., & O'Connor, W. P. (1988). Effect of a uniform sea level change on the Earth's rotation and gravitational field. *Geophysical Journal*, 93(1), 191–193. <https://doi.org/10.1111/j.1365-246X.1988.tb01398.x>
- Chen, J. L., Wilson, C. R., Hu, X. G., & Tapley, B. D. (2003). Large-scale mass redistribution in the oceans, 1993–2001. *Geophysical Research Letters*, 30(20), 9. <https://doi.org/10.1029/2003GL018048>
- Chen, X., & Wallace, J. M. (2016). Orthogonal PDO and ENSO indices. *Journal of Climate*, 29(10), 3883–3892. <https://doi.org/10.1175/JCLI-D-15-0684.1>
- Cheng, M. K., & Ries, J. (2018). Decadal variation in Earth's oblateness (J_2) from satellite laser ranging data. *Geophysical Journal International*, 212(2), 1218–1224. <https://doi.org/10.1093/gji/ggx483>
- Cheng, M. K., & Tapley, B. D. (1999). Seasonal variations in low degree zonal harmonics of the Earth's gravity field from satellite laser ranging observations. *Journal of Geophysical Research*, 104(B2), 2667–2681. <https://doi.org/10.1029/1998JB900036>
- Cheng, M. K., & Tapley, B. D. (2004). Variations in the Earth's oblateness during the past 28 years. *Journal of Geophysical Research*, 109, B09402. <https://doi.org/10.1029/2004JB003028>
- Cheng, M. K., Tapley, B. D., & Ries, J. C. (2013). Deceleration in the Earth's oblateness. *Journal of Geophysical Research: Solid Earth*, 118, 740–747. <https://doi.org/10.1002/jgrb.50058>

- Cox, C. M., & Chao, B. F. (2002). Detection of a large-scale mass redistribution in the terrestrial system since 1998. *Science*, 297(5582), 831–833. <https://doi.org/10.1126/science.1072188>
- Dickey, J. O., Marcus, S., de Viron, O., & Fukumori, I. (2002). Recent Earth oblateness variations: Unraveling climate and postglacial rebound effects. *Science*, 298(5600), 1975–1977. <https://doi.org/10.1126/science.1077777>
- Ding, H., & Chao, B. F. (2018). Application of stabilized AR-z spectrum in harmonic analysis for geophysics. *Journal of Geophysical Research: Solid Earth*, 123, 8249–8259. <https://doi.org/10.1029/2018JB015890>
- Kuang, W. J., Chao, B. F., & Chen, J. L. (2017). Decadal polar motion of the Earth excited by the convective outer core from geodynamo simulations. *Journal of Geophysical Research: Solid Earth*, 122, 8459–8473. <https://doi.org/10.1002/2017JB014555>
- Lavallée, D. A., Moore, P. M., Clarke, P. J., Petrie, E. J., van Dam, T., & King, M. A. (2010). J_2 : An evaluation of new estimates from GPS, GRACE, and load models compared to SLR. *Geophysical Research Letters*, 37, 14. <https://doi.org/10.1029/2010GL045229>
- Liau, J. R., & Chao, B. F. (2017). Variation of Antarctic Circumpolar Current and its intensification in relation to the Southern Annular Mode detected in the time-variable gravity signals by GRACE satellite. *Earth, Planets, Space*, 69. <https://doi.org/10.1186/s40623-017-0678-3>
- Loomis, B. D., Rachlin, K. E., & Luthcke, S. B. (2019). Improved Earth oblateness rate reveals increased ice sheet losses and mass-driven sea level rise. *Geophysical Research Letters*, 46, 6910–6917. <https://doi.org/10.1029/2019GL082929>
- Mathews, P. M., Herring, T. A., & Buffett, B. A. (2002). Modeling of nutation and precession: New nutation series for non-rigid Earth, and insights into the Earth's interior. *Journal of Geophysical Research*, 107(B4), ETG 3-1–ETG 3-26. <https://doi.org/10.1029/2001JB000390>
- Matsuo, K., Chao, B. F., Otsubo, T., & Heki, K. (2013). Accelerated ice mass depletion revealed by low-degree gravity field from satellite laser ranging: Greenland, 1991–2011. *Geophysical Research Letters*, 40, 4662–4667. <https://doi.org/10.1002/grl.50900>
- Melchior, P. (1989). The phase lag of Earth tides and the braking of the Earth's rotation. *Physics of the Earth and Planetary Interiors*, 56(3-4), 186–188. [https://doi.org/10.1016/0031-9201\(89\)90156-8](https://doi.org/10.1016/0031-9201(89)90156-8)
- Métris, G., Vokrouhlický, D., Ries, J. C., & Eanes, R. J. (1997). Nongravitational effects and the LAGEOS eccentricity excitations. *Journal of Geophysical Research*, 102(B2), 2711–2729. <https://doi.org/10.1029/96JB03186>
- Meyssignac, B., Lemoine, J. M., Cheng, M., Cazenave, A., Gégout, P., & Maisongrande, P. (2013). Interannual variations in degree-2 Earth's gravity coefficients $C_{2,0}$, $C_{2,2}$, and $S_{2,2}$ reveal large-scale mass transfers of climatic origin. *Geophysical Research Letters*, 40, 4060–4065. <https://doi.org/10.1002/grl.50772>
- Nerem, R. S., Chao, B. F., Au, A. Y., Chan, J. C., Klosko, S. M., Pavlis, N. K., & Williamson, R. G. (1993). Temporal variations of the Earth's gravitational field from satellite laser ranging to LAGEOS. *Geophysical Research Letters*, 20(7), 595–598. <https://doi.org/10.1029/93GL00169>
- Nerem, R. S., & Wahr, J. (2011). Recent changes in the Earth's oblateness driven by Greenland and Antarctic ice mass loss. *Geophysical Research Letters*, 38, 31. <https://doi.org/10.1029/2011GL047879>
- Petit, G., & Luzum, B. (2010). *IERS Conventions 2010, IERS Technical Note #36*. Frankfurt am Main: Verlag des Bundesamts für Kartographie und Geodäsie.
- Roy, K., & Peltier, W. R. (2011). GRACE era secular trends in Earth rotation parameters: A global scale impact of the global warming process? *Geophysical Research Letters*, 38, 26. <https://doi.org/10.1029/2011GL047282>
- Rubincam, D. P. (1984). Postglacial rebound observed by Lageos and the effective viscosity of the lower mantle. *Journal of Geophysical Research*, 89(B2), 1077–1087. <https://doi.org/10.1029/JB089iB02p01077>
- Rubincam, D. P. (1990). Drag on the Lageos satellite. *Journal of Geophysical Research*, 95(B4), 4881. <https://doi.org/10.1029/JB095iB04p04881>
- Seo, K., Chen, J., Wilson, C. R., & Lee, C. (2015). Decadal and quadratic variations of Earth's oblateness and polar ice mass balance from 1979 to 2010. *Geophysical Journal International*, 203(1), 475–481.
- Stacey, F. D., & Davis, P. M. (2008). *Physics of the Earth*. New York: Cambridge University Press.
- Thomson, D. J. (1982). Spectrum estimation and harmonic analysis. *Proceedings of the IEEE*, 70(9), 1055–1096. <https://doi.org/10.1109/PROC.1982.12433>
- Thompson, D. W. J., & Wallace, J. M. (2000). Annular modes in the extratropical circulation. Part I: Month-to-month variability. *Journal of Climate*. <https://doi.org/10.1175/1520-0442>
- Wahr, J., & Bergen, Z. (1986). The effects of mantle elasticity on nutations, Earth tides, and tidal variations in the rotation rate. *Geophysical Journal International*, 87(2), 633–668. <https://doi.org/10.1111/j.1365-246X.1986.tb06642.x>
- Woodworth, P. L. (2012). A note on the nodal tide in sea level records. *Journal of Coast Research*, 280, 316–323. <https://doi.org/10.2112/JCOASTRES-D-11A-00023.1>
- Wunsch, C., & Stammer, D. (1997). Atmospheric loading and the oceanic “inverted barometer” effect. *Reviews of Geophysics*, 35(1), 79–107. <https://doi.org/10.1029/96RG03037>
- Xu, C. Y., & Chao, B. F. (2019). Seismic effects on the secular drift of the Earth's rotational pole. *Journal of Geophysical Research*, 124, 6092–6100. <https://doi.org/10.1029/2018JB017164>
- Yoder, C. K., Williams, J. G., Dickey, J. O., Schutz, B. E., Eanes, R. J., & Tapley, B. D. (1983). Secular variations of Earth's gravitational harmonic J_2 coefficient from Lageos and non-tidal acceleration of Earth rotation. *Nature*, 303(5920), 757–762. <https://doi.org/10.1038/303757a0>
- Yu, J. Y., & Kao, H. Y. (2007). Decadal changes of ENSO persistence barrier in SST and ocean heat content indices: 1958–2001. *Journal of Geophysical Research*, 112, D13106. <https://doi.org/10.1029/2006JD007654>